iScience

Article

ANLN promotes head and neck squamous cell carcinoma progression by upregulating PD-L1 via the ERK-MAPK pathway

Graphical abstract

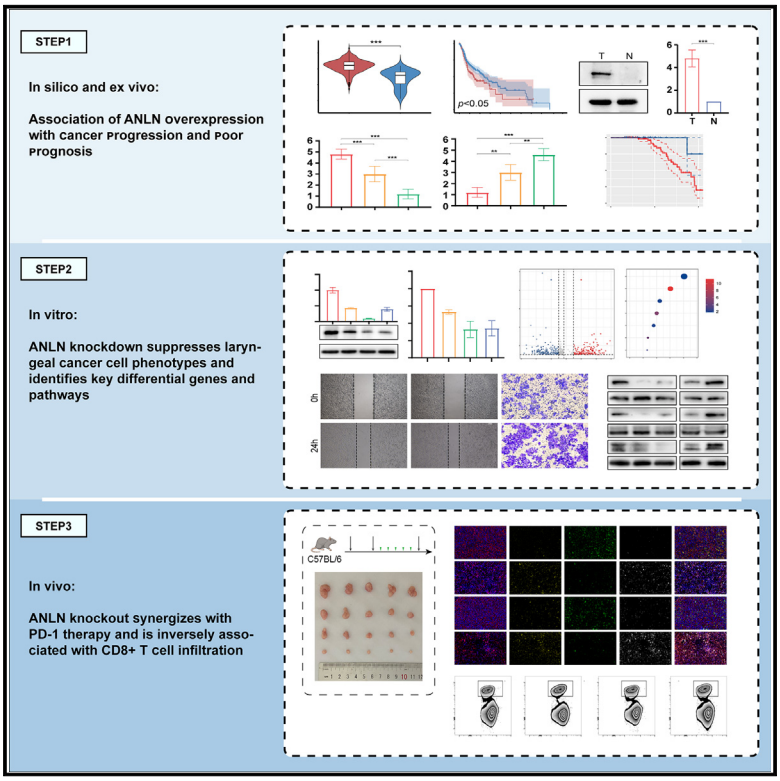

Highlights

- Silencing anillin (ANLN) inhibits HNSCC progression by reducing ERK-MAPK activation and PD-L1
- ANLN silencing reduces the tumor immune evasion by downregulating PD-L1 expression
- Combining ANLN silencing with anti-PD-1 therapy enhances $CD8^+$ T cell activation in HNSCC
- ANLN is a promising therapeutic target in HNSCC, supporting innovative combination treatments

Authors

Lei Wang, Junrong Wang, Nana Wang, ..., Hongxue Meng, Erliang Guo, Susheng Miao

Correspondence

guorliang@163.com (E.G.), drmiaosusheng@126.com (S.M.)

In brief

Molecular biology; Cell biology; Cancer

Wang et al., 2025, iScience *28*, 111633
February 21, 2025
https://doi.org/10.1016/j.isci.2024.111633

CellPress

iScience

CellPress
OPEN ACCESS

Article

ANLN promotes head and neck squamous cell carcinoma progression by upregulating PD-L1 via the ERK-MAPK pathway

Lei Wang,[1,8] Junrong Wang,[1,8] Nana Wang,[2,8] Xueying Wang,[3] Ming Song,[1] Yang Zhou,[4] Ziyuan Wang,[5] Hongxue Meng,[6] Erliang Guo,[7,9,*] and Susheng Miao[1,9,10,*]

[1]Department of Head and Neck Surgery, Harbin Medical University Cancer Hospital, Harbin 150081, Heilongjiang, P.R. China
[2]School of Public Health, Zhengzhou University, Zhengzhou 450001, Henan, P.R. China
[3]Department of Otolaryngology-Head and Neck Surgery, Xiangya Hospital, Central South University, No. 87 Xiangya Road, Changsha 410008, Hunan, P.R. China
[4]Department of Respiratory Medicine, Harbin Medical University Cancer Hospital, Harbin 150081, Heilongjiang, P.R. China
[5]Department of Pathology, Harbin Medical University, Harbin 150081, Heilongjiang, P.R. China
[6]Department of Pathology, Harbin Medical University Cancer Hospital, Harbin, Heilongjiang 150081, P.R. China
[7]Department of Thoracic Surgery, Harbin Medical University Cancer Hospital, Harbin 150081, Heilongjiang, P.R. China
[8]These authors contributed equally
[9]These authors contributed equally
[10]Lead contact
*Correspondence: guorliang@163.com (E.G.), drmiaosusheng@126.com (S.M.)
https://doi.org/10.1016/j.isci.2024.111633

SUMMARY

Anillin (ANLN) is a highly conserved protein involved in cytokinesis and cytoskeletal remodeling. This study investigates the role of ANLN in head and neck squamous cell carcinoma (HNSCC) progression and its impact on the tumor immune microenvironment, with a focus on the combination of ANLN silencing and anti-programmed cell death protein 1 (PD-1) therapy. Through *in vitro* and *in vivo* experiments, along with clinical specimen analysis, we discovered that silencing ANLN not only inhibits the malignant progression of HNSCC but also reduces the activation of the extracellular signal-regulated kinase-mitogen-activated protein kinase (ERK-MAPK) signaling pathway and decreases programmed death ligand-1 (PD-L1) expression. Integrating ANLN silencing with anti-PD-1 monoclonal antibody treatment significantly enhances the activation of infiltrating $CD8^+$ T cells, leading to marked tumor growth suppression. Our findings highlight the potential of ANLN as a therapeutic target in HNSCC, providing a foundation for developing innovative and effective combined treatment strategies.

INTRODUCTION

Head and neck squamous cell carcinoma (HNSCC) originates from the mucosal epithelial cells of the oral cavity, pharynx, and larynx.[1] Characterized by subtle initial symptoms, high rates of metastasis, and recurrence, this cancer type presents significant challenges in patient management.[2] Despite advancements in early detection and the implementation of multidisciplinary treatment approaches, the long-term survival rates for patients, especially those with lymph node metastases, remain disappointingly low. These observations underscore the urgent need for comprehensive research into the molecular underpinnings of tumor progression and the dynamics of the tumor immune microenvironment (TIME).[3] Moreover, developing more effective comprehensive treatment strategies is crucial.[4]

In recent years, the advancement of immune checkpoint blockade (ICB) research, particularly with programmed cell death protein 1 (PD-1) and programmed death ligand-1 (PD-L1) inhibitors, has led to their approval for managing recurrent or metastatic HNSCC.[5] However, the treatment faces challenges due to the infiltration of immunosuppressive cells and the scarcity of cytotoxic immune cells in HNSCC, resulting in many patients exhibiting a suboptimal response to these therapies.[6] This highlights the critical importance of exploring how intrinsic molecular characteristics interact with host immune responses within the HNSCC TIME.

Building on this, there is an urgent need for detailed research to further understand the complex interactions between these molecular characteristics and the host immune responses within the HNSCC TIME. Dysregulation of ANLN in certain cancers[7,8] has been linked to abnormal cell cycle[9,10] and cytoskeletal remodeling,[11,12] potentially hastening tumor progression.[13–17] Elevated ANLN expression in cancers such as breast,[18,19] lung,[20] gastric,[21] and colorectal[22] has been associated with enhanced cancer cell invasion and metastasis.[23] Our previous study explored and found that selectively spliced ANLN isoforms synergistically promote the progression of HNSCC.[24]

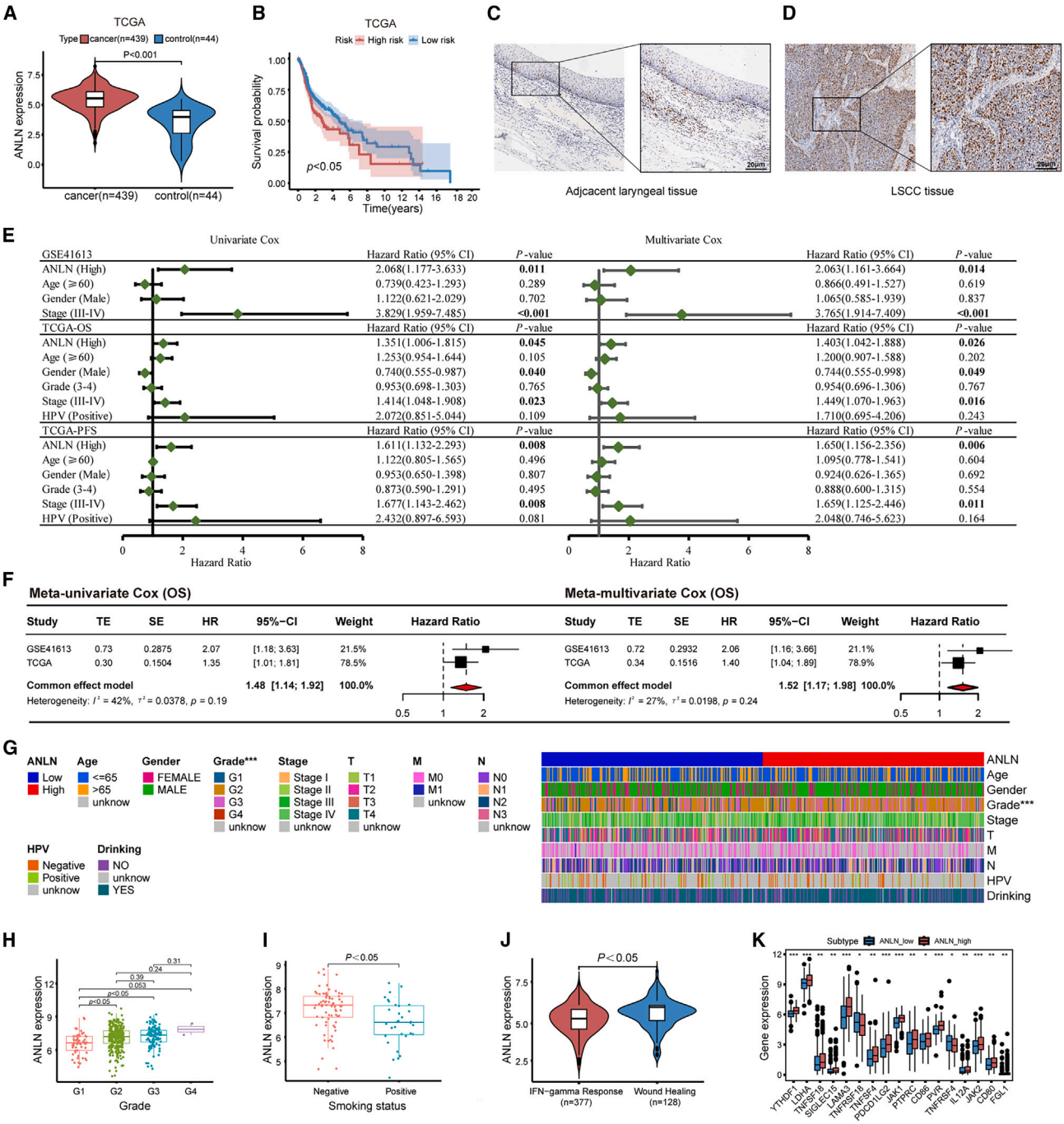

Figure 1. Expression and prognostic analysis of ANLN in HNSCC

(A) Expression levels of ANLN in the TCGA-HNSCC cohort.

(B) Survival analysis comparing high and low ANLN expression groups in the TCGA cohort.

(C and D) Immunohistochemistry (IHC) staining for ANLN in adjacent non-tumor tissues (C) and LSCC tissues (D).

(E) Univariate and multivariate Cox regression analyses of ANLN expression.

(F) Meta-analysis of the prognostic significance of ANLN expression in the GSE41613 and TCGA cohorts.

(G) Correlation of ANLN expression with various clinicopathologic features, including HNSCC subtypes.

(H) Boxplot showing the distribution of ANLN expression across different LSCC tumor grades.

(I) Boxplot comparing ANLN expression levels in LSCC patients with different smoking statuses.

(J) Comparison of ANLN expression levels with IFNγ mutation status.

(K) Boxplot illustrating the differential expression of immune checkpoint genes between high and low ANLN expression groups in HNSCC from the TCGA dataset.

*Statistical significance is denoted as *p < 0.05, **p < 0.01, ***p < 0.001. Data are represented as mean with SD.

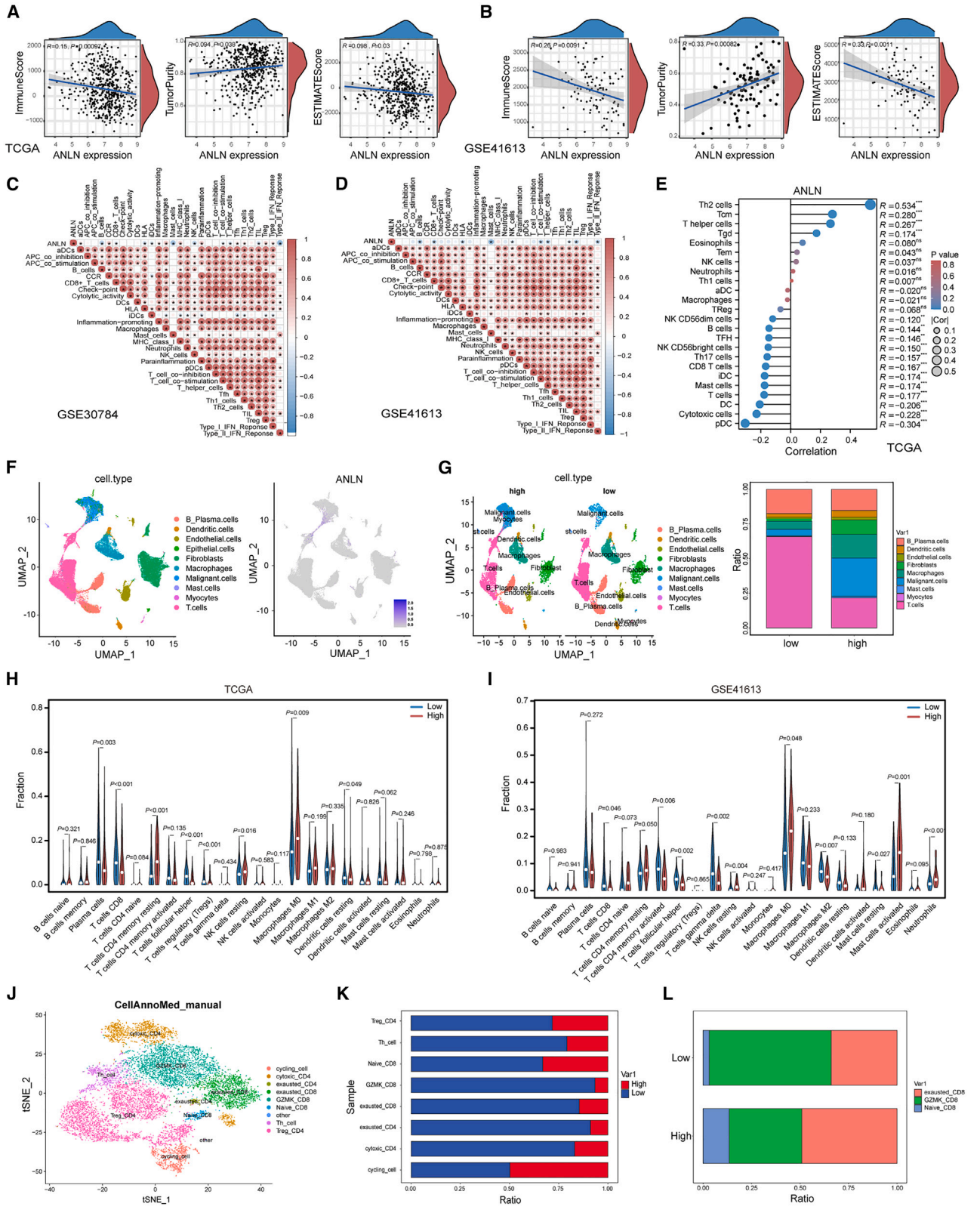

(legend on next page)

However, ANLN's specific role in the HNSCC TIME is yet to be clearly defined. This study establishes a significant association between ANLN expression and CD8 cytotoxic T cell presence in HNSCC tissues, highlighting the importance of $CD8^+$ T cells in the immune response within the HNSCC TIME.[25] Modulating the TIME to encourage $CD8^+$ T cell infiltration and activation could improve treatment outcomes for HNSCC patients.[26] Therefore, understanding the TIME and the dynamics of $CD8^+$ T cells in HNSCC is essential for developing effective treatment strategies and improving subsequent clinical outcomes.

In this study, we validated the critical role of ANLN in the malignant progression of HNSCC and provided empirical support for the ANLN-regulated ERK-MAPK signaling pathway and PD-L1 protein levels. Our research revealed that ANLN enhances the *in vitro* migratory ability and *in vivo* proliferative capacity of head and neck tumor cell lines. A negative correlation between ANLN expression and $CD8^+$ T cell infiltration was also observed. Consequently, this study highlights the importance of silencing ANLN in combination with anti-PD-1 monoclonal antibody therapy in HNSCC, leveraging a synergistic effect to enhance the efficacy of immunotherapy. Our research deepens the understanding of TIME regulation and protein expression mechanisms related to anti-tumor immune responses, thus laying the groundwork for developing innovative and specific therapeutic targets and combined treatment strategies.

RESULTS

Focusing on ANLN in HNSCC through comprehensive analyses

ANLN expression levels were significantly higher in HNSCC tissues compared to adjacent non-cancerous tissues, as analyzed from the TCGA-HNSCC cohort (Figure 1A). Similar results were observed across the TCGA pan-cancer dataset and the GEO dataset (GSE442743) (Figures S1A and S1B). In the TCGA-HNSCC cohorts, we divided the samples into high- and low-expression groups based on the median ANLN expression level. Notably, high ANLN expression was associated with a poorer survival prognosis in HNSCC (Figures 1B and S1C). Consistent findings were observed in other cancer types, including kidney, lung, liver, melanoma, and uroepithelial cancers (Figure S1D). The expression level of ANLN was significantly higher in laryngopharyngeal squamous cell carcinoma (LSCC) tumor cells compared to adjacent normal tissue cells (Figures 1C and 1D).

In a multivariate Cox proportional hazards regression model, ANLN expression was identified as an independent prognostic factor for both overall survival (OS) and progression-free survival (PFS) in the TCGA and GSE41613 cohorts (Figure 1E). We further conducted a prognostic meta-analysis of the TCGA and GSE41613 datasets to evaluate the predictive value of ANLN expression on patient prognosis (Figure 1F).

We also examined the correlation between ANLN expression and clinicopathological features in HNSCC. ANLN expression was significantly associated with tumor histologic grade, new tumor event status, and sample type (Figure 1G). Moreover, ANLN expression increased significantly in higher pathological grades (Figure 1H), smoking status (Figure 1I), and was positively correlated with interferon gamma (IFNγ) expression and wound-healing-related processes (Figure 1J). Figure 1K illustrates the expression levels of immune-checkpoint-related genes between the ANLN_low and ANLN_high subgroups. The boxplots indicate significantly higher expression of genes such as LDHA, TNFRSF18, PDCD1LG2, and LAMA3 in the ANLN_high subgroup compared to the ANLN_low group ($p < 0.05$), suggesting distinct immune checkpoint gene expression profiles between the two groups (Figure 1K).

Exploring the impact of ANLN on immune cell infiltration in the HNSCC TIME

To enhance the understanding of ICB therapy efficacy in HNSCC patients, we analyzed the TCGA (Figure 2A) and GSE41613 (Figure 2B) datasets. ANLN expression was found to negatively correlate with immune score and ESTIMATE scores, while positively correlating with tumor purity. This suggests that higher ANLN expression may reduce immune cell infiltration in the tumor microenvironment, thus potentially impacting the effectiveness of ICB therapy. Next, we explored the relationship between ANLN expression and immune cell infiltration levels. Increased ANLN expression was associated with a significant reduction in the abundance of $CD8^+$ T cells and other immune cells across the GSE30784 (Figure 2C), GSE41613 (Figure 2D), and TCGA (Figure 2E) datasets ($p < 0.05$).

Using scRNA-seq data from Kim et al.'s HNSCC atlas (GSE181919),[27] we identified that ANLN is primarily expressed

Figure 2. Correlation between ANLN expression and immune cell infiltration in HNSCC tumor immune microenvironment (TIME)

(A) Correlation plots showing the relationship between ANLN expression and immune-related scores (stromal, immune, and ESTIMATE scores) in the TCGA dataset. Higher ANLN expression is associated with lower immune and stromal scores.

(B) Similar correlation plots for the GSE41613 dataset.

(C and D) Heatmaps showing the correlation between ANLN expression and the infiltration levels of various immune cell types in the GSE30784 (C) and GSE41613 (D) datasets.

(E) Dot plot showing the correlation between ANLN expression and multiple immune checkpoint genes in the TCGA dataset.

(F and G) UMAP plots showing the distribution of different immune cell types and ANLN expression in the HNSCC tumor microenvironment, based on single-cell RNA sequencing (scRNA-seq) data from the HNSCC atlas (GSE181919).

(H and I) Bar plots comparing the relative abundance of various immune cell types between high and low ANLN expression groups in the TCGA (H) and GSE41613 (I) datasets.

(J) UMAP plot from scRNA-seq analysis.

(K) Proportional comparison of immune cell subtypes between high and low ANLN expression groups.

(L) Stacked bar plots showing the proportions of different immune cell subtypes in the high and low ANLN expression groups. *Statistical significance is denoted as $^*p < 0.05$, $^{**}p < 0.01$, $^{***}p < 0.001$. Data are represented as mean with SD.

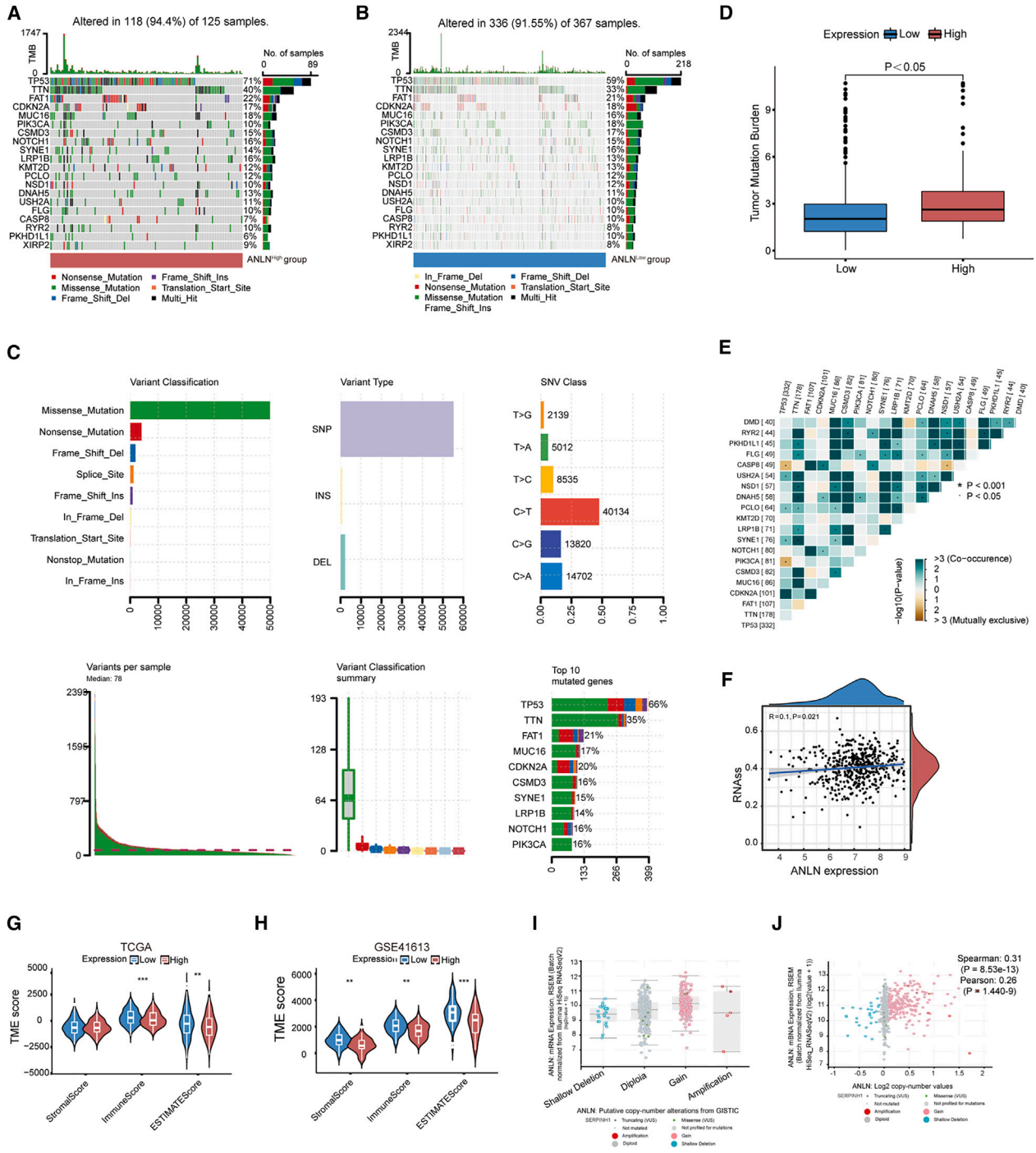

Figure 3. Impact of ANLN on tumor progression and genomic alterations in LSCC and its clinical significance

(A and B) Oncoplot showing the distribution of genomic alterations in high (A) and low (B) ANLN expression groups from the TCGA dataset.

(C) Bar graphs illustrating the variant classification, variant type, and single nucleotide variant (SNV) count across samples.

(D) Boxplot comparing tumor mutational burden (TMB) between high and low ANLN expression groups.

(E) Heatmap of the correlation between ANLN expression and stemness-related driver genes.

(F) Correlation plot depicting the positive association between ANLN expression and stemness RNA levels.

(G and H) Violin plots comparing stromal scores between high and low ANLN expression groups in the TCGA (G) and GSE41613 (H) datasets.

(I) Analysis of genomic variations in ANLN.

(J) Scatterplot showing a significant positive correlation between ANLN copy-number variations (CNVs) and mRNA expression levels ($p < 0.01$). *Statistical significance is denoted as follows: *$p < 0.05$, **$p < 0.01$, ***$p < 0.001$. Data are represented as mean with SD.

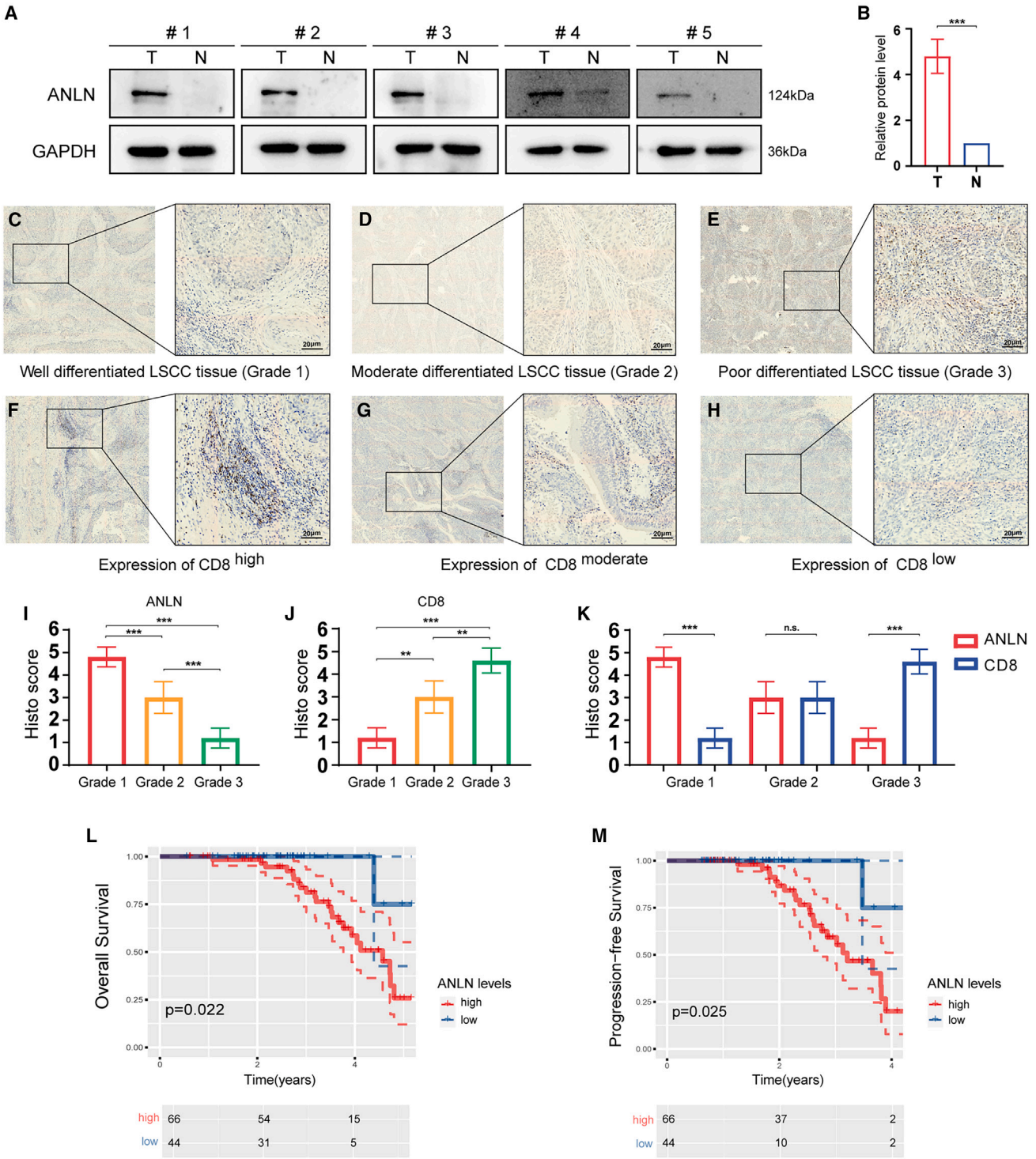

Figure 4. ANLN expression and its correlation with tumor differentiation and prognosis in LSCC tissues

(A) Western blot analysis of ANLN expression in LSCC tissues (T) and adjacent non-tumor tissues (N).

(B) Quantification of ANLN expression levels in tumor versus non-tumor tissues.

(C–E) Immunohistochemistry (IHC) staining for ANLN in LSCC tissues with varying differentiation levels: well-differentiated (Grade 1) (C), moderately differentiated (Grade 2) (D), and poorly differentiated (Grade 3) (E) tissues.

(F–H) IHC staining for CD8$^+$ T cells in LSCC tissues with different levels of differentiation: high CD8$^+$ infiltration (F), moderate CD8$^+$ infiltration (G), and low CD8$^+$ infiltration (H).

(legend continued on next page)

in T cells[28,29] (Figure 2F). When samples were divided into high and low ANLN expression groups based on the median expression, we observed a significant reduction in T cell infiltration in the high ANLN group (Figure 2G). To further investigate ANLN's impact on T cell subtypes, we analyzed the relationship between ANLN expression and 22 immune cell subtypes using the TCGA (Figure 2H) and GSE41613 (Figure 2I) datasets. High ANLN expression was significantly associated with lower levels of $CD8^+$ T cells and helper T cells ($p < 0.01$), and it also influenced cytokine and chemokine signaling in the tumor immune microenvironment (Figures S2A–S2D).

In the scRNA-seq dataset (GSE181919), T cells were clustered into eight distinct groups based on classical biomarkers (Figures 2J and 2K). Our analysis revealed that ANLN expression was inversely correlated with T cell infiltration. Notably, in the high ANLN expression group, there was a predominance of exhausted $CD8^+$ T cells, whereas the low ANLN expression group had higher proportions of GZMK-expressing $CD8^+$ T cells, which are typically associated with effective anti-tumor immune responses (Figure 2L).

Exploring the impact of ANLN in shaping the TIME and predicting tumor progression and clinical response to ICB treatment

We analyzed tumor mutational burden (TMB) in both high and low ANLN expression groups using the TCGA datasets. High ANLN expression was significantly associated with frequent mutations in key genes such as TP53 and TTN (Figures 3A and 3B). Missense mutations were the most prevalent genomic variant (Figure 3C). Patients in the high ANLN expression group exhibited significantly higher TMB values compared to the low expression group (Figure 3D). Furthermore, we explored the interactions among 20 driver genes and found a positive correlation between ANLN expression and stemness RNA, indicating a potential role of ANLN in tumorigenesis (Figures 3E and 3F). In the TCGA dataset (Figure 3G), no statistically significant difference was observed between low and high ANLN expression with respect to stromal scores. However, high ANLN expression was linked to significantly lower immune ($p < 0.001$) and ESTIMATE scores ($p < 0.01$). In contrast, in the GSE41613 dataset (Figure 3H), significant differences were found across all three scores, with high ANLN expression associated with lower stromal ($p < 0.01$), immune ($p < 0.01$), and ESTIMATE scores ($p < 0.001$). These results suggest that ANLN's impact on the tumor microenvironment (TME) may vary depending on the dataset, with stromal scores being significant only in the GSE41613 cohort.

Analysis of ANLN's genomic variations revealed shallow deletions, diploid status, copy number gains, and amplifications (Figure 3I). The copy number of ANLN was significantly correlated with its mRNA expression level (Figure 3J). Additionally, $CD8^+$ T cell infiltration was found to be significantly associated with ANLN copy-number variations (CNVs), highlighting its potential role in immune modulation. Across various cancers, TMB exhibited a strong positive correlation with ANLN expression in KICH, STAD, and SARC, whereas ANLN expression was positively correlated with microsatellite instability (MSI) in ACC, UCEC, STAD, and SARC (Figures S2E–S2H). We further analyzed ANLN mutation sites and their corresponding case numbers, alongside the localization of ANLN's CNVs on chromosomes (Figure S2I). Finally, we identified a significant positive correlation between ANLN mRNA expression levels and methylation at the cg17401719 and cg00267323 probes, whereas a negative correlation was observed at the cg04897631 probe (Figure S2J).

High ANLN expression indicates poorer prognosis in HNSCC

ANLN was highly expressed in HNSCC tissues and associated with poor prognosis by TCGA-HNSCC cohort analysis. To further investigate this, we analyzed ANLN protein expression in samples from 110 patients with radically resected LSCC using western blotting and immunohistochemistry (IHC). ANLN expression was significantly higher in LSCC tissues compared to adjacent non-tumor tissues (Figures 4A and 4B). IHC results showed that among 66 HNSCC patients, ANLN was highly expressed in tumor tissues, whereas 44 patients had low ANLN expression. High ANLN expression correlated with patient age, tumor grading, pN0 status, lymph node metastasis, and $CD8^+$ T cell levels (Figures 4C–4M and S2K–S2M; Table S1).

IHC analyses of HNSCC tissues revealed that higher tumor grading correlated with high ANLN expression and low $CD8^+$ T cell infiltration, whereas lower tumor grading was associated with low ANLN expression and high $CD8^+$ T cell infiltration (Figures 4C–4K). Therefore, ANLN expression in LSCC tissues demonstrated a significant negative correlation with $CD8^+$ T cell infiltration. Kaplan-Meier analysis indicated that patients with high ANLN expression had significantly shorter OS and PFS compared to those with low ANLN expression (Figures 4L and 4M).

ANLN promotes the migration of HNSCC cells *in vitro*

We aimed to investigate the expression of ANLN in HNSCC cell lines and to construct cell lines with silenced and overexpressed ANLN. The transcriptional and protein levels of ANLN in different HNSCC cell lines were examined using RT-qPCR and western blotting. Consistently, ANLN levels were significantly higher in all HNSCC cell lines compared to the NOK cell line. Furthermore, ANLN was highly expressed in AMC-HN-8 cells compared to SCC-4 cells (Figure 5A). Statistical analysis indicated significant differences in ANLN expression between these cell lines. Consequently, we selected the human LSCC cell line AMC-HN-8 and the commonly used human tongue squamous cell carcinoma

(I and J) Quantification of ANLN (I) and $CD8^+$ T cell (J) expression across different LSCC tumor grades.
(K) Comparative analysis of ANLN and $CD8^+$ T cell expression across various tumor grades.
(L) Kaplan-Meier survival analysis showing overall survival (OS) of LSCC patients stratified by ANLN expression levels.
(M) Kaplan-Meier survival analysis showing progression-free survival (PFS) of LSCC patients stratified by ANLN expression levels. Patients with high ANLN expression exhibited significantly shorter PFS compared to those with low ANLN expression ($p = 0.025$). *Statistical significance is indicated as follows: $^*p < 0.05$, $^{**}p < 0.01$, $^{***}p < 0.001$. Data are represented as mean with SD.

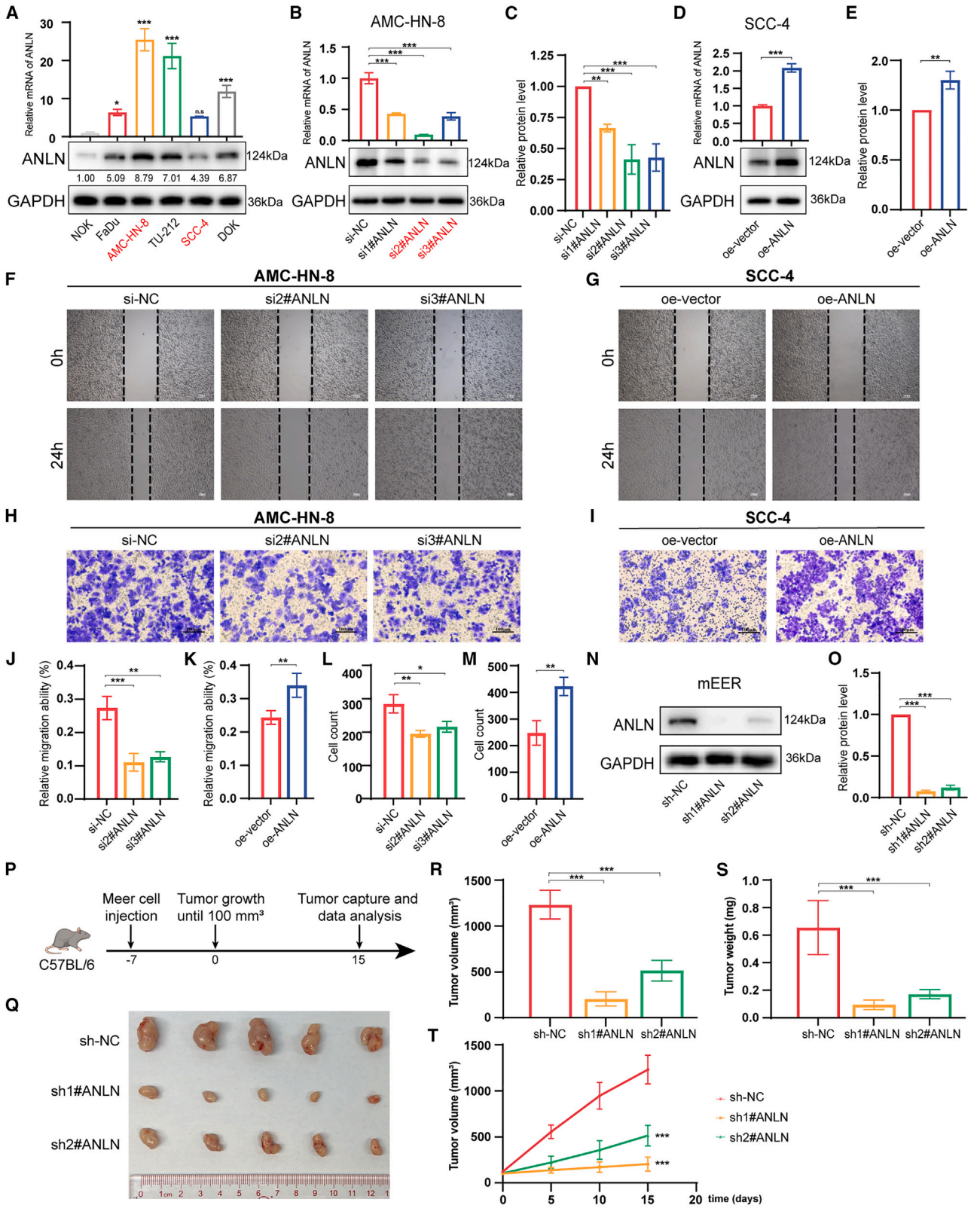

(legend on next page)

cell line SCC-4 for further studies. ANLN small interfering RNA (si-ANLN) and ANLN-cDNA (oe-ANLN), along with their respective negative controls (si-NC and oe-vector), were successfully transfected into human HNSCC cell lines (Figures 5B–5E).

ANLN exhibits a malignant phenotype in various tumors. To explore its functional role in the progression of HNSCC, we first conducted wound healing assays. The findings indicated that silencing ANLN significantly inhibited the migration of AMC-HN-8 cells (Figures 5F and 5J), whereas overexpression of ANLN significantly promoted the migration of SCC-4 cells (Figures 5G and 5K), suggesting that ANLN enhances the migration of HNSCC cells. Further evidence was provided by Transwell migration assays, demonstrating that inhibiting ANLN expression impaired the migratory potential of HNSCC cells (Figures 5H and 5L). Moreover, overexpressing ANLN in SCC-4 cells substantially increased their migration ability (Figures 5I and 5M). In summary, these results suggest that ANLN actively promotes the migration of HNSCC cells *in vitro*.

ANLN promotes HNSCC growth *in vivo*

After establishing the role of ANLN in promoting HNSCC cell migration *in vitro*, we aimed to further evaluate its impact on HNSCC tumor growth *in vivo*. ANLN short hairpin RNA (sh-ANLN) and their negative controls (sh-NC) were successfully transfected into mouse HNSCC cell lines (mEER) (Figures 5N and 5O). To assess the *in vivo* function of ANLN, we established a xenograft mouse model using mEER cells (Figure 5P). mEER cells and ANLN-deficient mEER cells were subcutaneously transplanted into C57BL/6 mice, and the tumor volume and weight were significantly reduced in the ANLN knockout group compared to the control group (Figures 5Q–5T). Our data suggest that ANLN actively promotes HNSCC tumor growth *in vivo*.

ANLN regulates the MAPK/ERK signaling pathway

To investigate the regulatory mechanisms, we conducted bioinformatics analysis to predict potentially related signaling pathways. Based on the differential genes identified in the high and low ANLN expression groups in the TCGA-HNSCC cohort, our GSEA analysis revealed that the enriched pathways included cell cycle, mitosis, and MAPK activation, among others (Figure 6A). Additionally, we analyzed T lymphocytes in the GSE181919 scRNA-seq cohort, categorizing them into high and low ANLN expression groups and identifying differential genes. Reactome analysis indicated that the predominant enriched pathways included MAPK-related pathways, cell-cycle regulation, and hypoxia-related pathways (Figure 6B).

AMC-HN-8 cell lines with si-ANLN and siNC were analyzed for RNA sequences and differentially expressed genes. Red represents upregulated genes, and blue represents downregulated genes (Figure 6C). Subsequent GSEA analysis revealed that the enriched pathways included the MAPK signaling pathway, cell cycle, MTOR signaling pathway, and TNF signaling pathway (Figure 6D). These results suggest that ANLN may regulate the MAPK/ERK signaling pathway.

ANLN promotes PD-L1 expression by activating the MAPK/ERK signaling pathway

The MAPK/ERK pathway is crucial in the developing various cancers.[30,31] To assess the regulatory effects of ANLN on the MAPK/ERK signaling pathway, we examined the expression levels of essential proteins and their phosphorylated forms after interfering with ANLN expression using western blotting. Our findings indicated that in siANLN-transfected AMC-HN-8 cells, the expression of p-MEK and p-ERK1/2 was significantly reduced compared to the siNC group (Figure 6E). Conversely, overexpression of ANLN in SCC4 cells resulted in a significant increase in the expression of p-MEK and p-ERK1/2. Notably, ANLN expression had almost no effect on the total MEK and ERK1/2 protein levels in AMC-HN-8 and SCC4 cells (Figure 6E).

To explore whether ANLN regulates PD-L1 expression through the MAPK/ERK signaling pathway,[32] we used TBHQ (an ERK1/2 activator) and overexpressed ANLN to activate MAPK/ERK signaling, whereas AZD-0364 (an ERK1/2 inhibitor) and ANLN knockdown were used to inhibit this pathway.[33] To explore whether ANLN regulates PD-L1 expression through the MAPK/ERK signaling pathway, western blotting results showed that TBHQ partially reversed the downregulation of p-ERK1/2 and PD-L1 expression caused by ANLN knockdown in AMC-HN-8 cells. Similarly, AZD-0364 partially reversed the upregulation of p-ERK1/2 and PD-L1 expression caused by ANLN overexpression in SCC-4 cells (Figure 6F). Thus, we conclude that ANLN can activate the MAPK/ERK signaling pathway and affect PD-L1 expression.

Lack of ANLN *in vivo* has a synergistic effect with anti-PD-1 monoclonal antibody treatment

We have established that ANLN regulates PD-L1 expression via the MAPK/ERK signaling pathway. The *in vivo* experimental

Figure 5. ANLN promotes migration and growth of HNSCC cells

(A) RT-qPCR and western blot analysis of ANLN expression in various HNSCC cell lines compared to NOK cells.

(B–E) Successful transfection of ANLN small interfering RNA (si-ANLN) and ANLN-cDNA (oe-ANLN) into human HNSCC cell lines, alongside their respective negative controls (si-NC and oe-vector). Confirmation of ANLN knockdown and overexpression was verified by RT-qPCR and western blot.

(F and J) Wound healing assay showing that ANLN silencing significantly impairs the migration of AMC-HN-8 cells.

(G and K) Wound healing assay demonstrating that ANLN overexpression significantly enhances the migration of SCC-4 cells.

(H and L) Transwell migration assay confirming that inhibiting ANLN expression reduces the migratory ability of HNSCC cells.

(I and M) Transwell migration assay indicating that overexpression of ANLN in SCC-4 cells substantially promotes their migration capacity.

(N and O) Successful transfection of ANLN short hairpin RNA (sh-ANLN) and negative control (sh-NC) into mouse HNSCC cell lines (mEER), with RT-qPCR and western blot confirming ANLN knockdown.

(P) Establishment of a xenograft mouse model using mEER cells. mEER cells and ANLN-deficient mEER cells were transplanted subcutaneously into C57BL/6 mice.

(Q–T) Tumor volume and weight measurements. *Statistical significance is represented as $^{*}p < 0.05$, $^{**}p < 0.01$, $^{***}p < 0.001$. Data are represented as mean with SD.

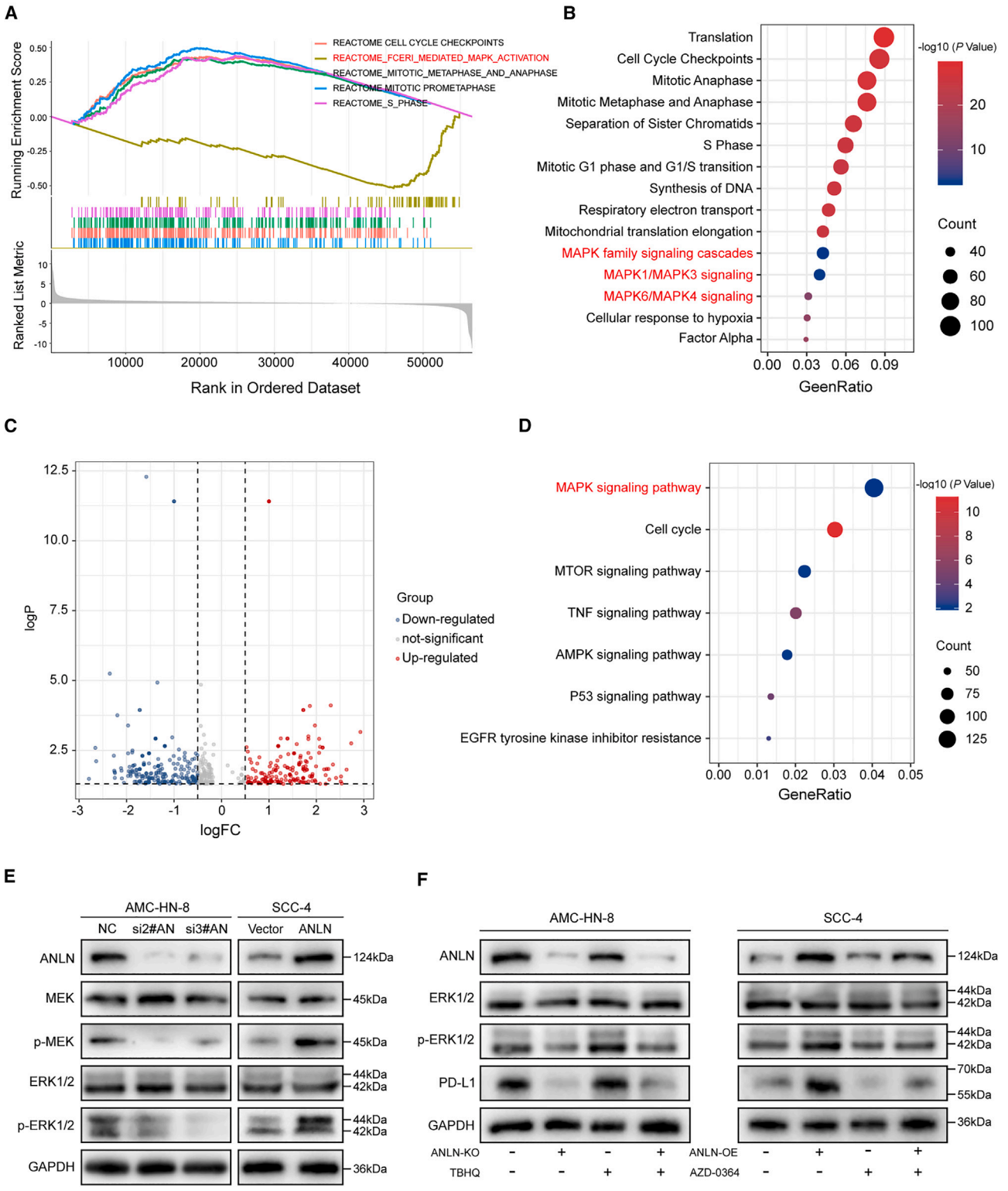

Figure 6. ANLN regulates the MAPK/ERK signaling pathway and PD-L1 expression

(A) Gene set enrichment analysis (GSEA) of differentially expressed genes between high and low ANLN expression groups from the TCGA-HNSCC cohort.

(B) Reactome pathway analysis of T lymphocytes from the GSE181919 scRNA-seq cohort.

(legend continued on next page)

procedure and treatment regimen are depicted in Figure 7A. Before immunotherapy, subcutaneous head and neck tumor models were established using Anln-deficient mEER cells and the mEER cell line. Afterward, the tumor-bearing mice were treated with anti-PD-1 monoclonal antibody and immunoglobulin G2a (IgG2a) control. Anti-mouse PD-1 antibody treatment significantly reduced tumor volume and weight compared to the homologous mouse IgG2a group inoculated with the same cells (Figures 7B–7E). Of greater significance, compared to monotherapy, the combination therapy of Anln knockdown with anti-mouse PD-1 antibody demonstrated the most substantial anti-tumor effect (Figure 7B). This indicates that although anti-PD-1 monotherapy can partially alleviate the tumor burden, the combined treatment of Anln knockdown with anti-mouse PD-1 antibody has the potential to exert a synergistic effect, thereby further enhancing the efficacy of immunotherapy and exerting a more pronounced inhibitory effect on tumors. Additionally, we assessed the body weight of mice across different treatment groups to ensure no adverse effects on overall health. The results showed no significant difference in body weight among the groups (Figure 7E).

To gain deeper insight into the proportion of $CD8^+$ T cells and their cytotoxic marker GZMB in different treatment groups, we conducted multiplex IHC (mIHC) analysis on mouse tumor samples with immunological activity. The resulting multiplex immunofluorescence analysis revealed that the loss of Anln led to a significant increase in the infiltration density and activity (GZMB+) of $CD8^+$ T cells. The increase was particularly notable in the combination treatment group, which exhibited the highest levels of $CD8^+$ T cell infiltration and GZMB expression (Figure 7F).

Our data suggest that Anln is a potential therapeutic target in HNSCC. Silencing Anln enhances anti-tumor immunity by recruiting more cytotoxic immune cells, inhibiting HNSCC growth. Furthermore, we successfully enhanced the efficacy of anti-PD-1 treatment. Flow cytometry analysis further confirmed that the combination treatment group had the highest proportion of killer active CD8 (GZMB+) cells and a lower proportion of exhaustion $CD8^+$ (PD-1+) cells (Figures 7G–7I). These results suggest a synergistic effect of targeting ANLN combined with immunotherapy.

DISCUSSION

This study comprehensively explores the role of ANLN in HNSCC progression and its impact on immunotherapy using cellular experiments, clinical samples, and external datasets. Our findings are consistent with the existing literature, indicating that high ANLN expression in HNSCC is linked to poor prognosis and shorter overall survival. Techniques such as western blotting and immunohistochemical staining further confirmed the positive correlation between ANLN expression and malignant progression. Additionally, we observed a negative correlation between ANLN expression and $CD8^+$ T cell infiltration in HNSCC tissues. As ANLN expression increases, the infiltration of various immune cells and the expression of immunological markers decline, suggesting an immunosuppressive tumor microenvironment.

Using scRNA-seq data, we categorized HNSCC samples into high and low ANLN expression groups and observed significant differences in immune cell populations. Specifically, the low ANLN group had a higher proportion of GZMK_CD8 T cells, whereas the high ANLN group was dominated by exhausted $CD8^+$ T cells. These differential gene expressions were closely associated with the MAPK signaling pathway, which is known to play a crucial role in malignant tumor progression. We further validated the relationship between ANLN and PD-L1 expression in HNSCC cells, reinforcing the potential of ANLN as a therapeutic target.

However, the clinical application of targeting ANLN faces several challenges. The broad expression of ANLN across different tissues raises concerns about specificity and potential off-target effects. Moreover, although our *in vivo* experiments demonstrated that ANLN knockdown enhances $CD8^+$ T cell infiltration and improves the tumor immune microenvironment, further studies are needed to develop specific small molecule inhibitors targeting ANLN and to assess their clinical efficacy and safety.

Despite the current limitations in immunotherapy efficacy, with response rates to immune checkpoint inhibitor (ICI) treatments being only 16%, enhancing $CD8^+$ T cell infiltration into the tumor microenvironment may improve outcomes in late-stage HNSCC patients. Our experiments showed that ANLN knockdown, in combination with anti-PD-1 therapy, results in a synergistic anti-tumor effect, both improving $CD8^+$ T cell infiltration and reducing PD-L1 expression. This combination strategy holds great promise for future therapeutic development.

Limitations of the study

First, the development of small molecule inhibitors targeting ANLN might offer a complementary approach to improve clinical outcomes. Second, although the preclinical data are promising, additional validation through larger, multi-center clinical trials is needed to confirm the broader applicability of these findings across different patient populations.

RESOURCE AVAILABILITY

Lead contact

Further information and requests for resources and reagents should be directed to and will be fulfilled by the lead contact, Professor Susheng Miao (drmiaosusheng@126.com).

(C) RNA sequencing analysis of AMC-HN-8 cell lines transfected with si-ANLN or si-NC, showing differentially expressed genes. Upregulated genes are marked in red, whereas downregulated genes are shown in blue.

(D) GSEA of differentially expressed genes in AMC-HN-8 cells treated with si-ANLN, revealing enriched pathways such as MAPK signaling, cell cycle, mTOR signaling, and TNF signaling.

(E) Western blot analysis of phosphorylated MEK (p-MEK), phosphorylated ERK1/2 (p-ERK1/2), and total MEK and ERK1/2 protein levels in si-ANLN-transfected AMC-HN-8 cells and ANLN-overexpressed SCC-4 cells.

(F) Western blot analysis illustrating the effects of TBHQ (an ERK1/2 activator) and AZD-0364 (an ERK1/2 inhibitor) on p-ERK1/2 and PD-L1 expression. *Statistical significance is represented as $^*p < 0.05$, $^{**}p < 0.01$, $^{***}p < 0.001$. Data are represented as mean with SD.

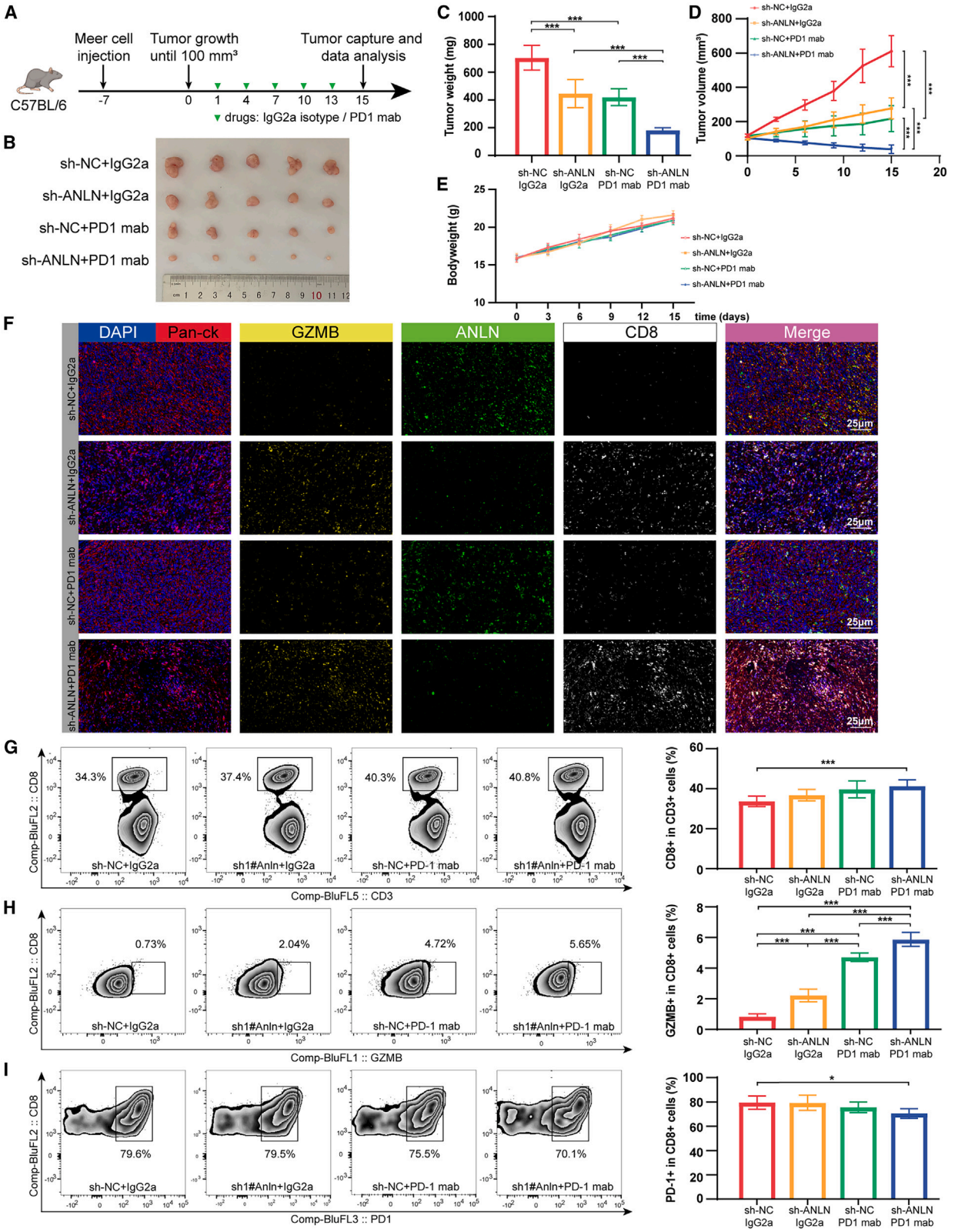

(legend on next page)

Materials availability

This work did not result in new unique reagents. The primer sequences used are available on request from the corresponding author.

Data and code availability

The whole-transcriptome data and clinical characteristics of head and neck squamous cell carcinoma (HNSCC) were acquired from The Cancer Genome Atlas (TCGA) project (https://portal. gdc. cancer. gov/). From the Gene-Expression Omnibus (GEO) databases, HNSC datasets (GSE41613, GSE30784) were enrolled. The data reported in this paper will be shared upon request to the lead corresponding author (drmiaosusheng@126.com). This paper dose not report original code. Any additional information required to reanalyze the data reported in this paper is available from the lead contact upon request.

ACKNOWLEDGMENTS

The authors disclosed receipt of the following financial support for the research, authorship, and/or publication of this article. This work was supported by the Natural Science Foundation of Heilongjiang Province, China (07000044); Beijing Medical Award Foundation (YXJL-2021-0613-0447); Harbin Medical University Cancer Hospital Climbing Plan Project (PDYS2024-09); and Research Project on Basic Research Funds for Provincial Universities in Heilongjiang Province in 2023 (2023-KYYWF-0216).

AUTHOR CONTRIBUTIONS

L.W., writing—original draft, methodology, formal analysis, conceptualization, and writing—review & editing. J.W., methodology, investigation, formal analysis, and data curation. N.W., software, resources, formal analysis, and data curation. X.W., formal analysis, methodology, and writing—review & editing. M.S., methodology, investigation, formal analysis, and data curation. Y.Z., methodology, investigation, formal analysis, and data curation. Z.W., visualization, validation, software, resources, and methodology. H.M., visualization, validation, software, resources, and methodology. E.G., writing—review & editing, supervision, and funding acquisition. S.M., writing—review & editing, supervision, funding acquisition, and conceptualization.

DECLARATION OF INTERESTS

The authors declare no competing interests.

STAR★METHODS

Detailed methods are provided in the online version of this paper and include the following:

SUPPLEMENTAL INFORMATION

Supplemental information can be found online at https://doi.org/10.1016/j.isci.2024.111633.

Received: May 26, 2024
Revised: September 27, 2024
Accepted: December 16, 2024
Published: December 18, 2024

REFERENCES

1. Wallington, D.G., Contessa, J.N., and Hayman, T.J. (2022). STING Agonists in Head and Neck Squamous Cell Carcinoma. Cancer J. *28*, 401–406.
2. Johnson, D.E., Burtness, B., Leemans, C.R., Lui, V.W.Y., Bauman, J.E., and Grandis, J.R. (2020). Head and neck squamous cell carcinoma. Nat. Rev. Dis. Primers *6*, 92.
3. Solomon, B., Young, R.J., and Rischin, D. (2018). Head and neck squamous cell carcinoma: Genomics and emerging biomarkers for immunomodulatory cancer treatments. Semin. Cancer Biol. *52*, 228–240.
4. Shi, Y., Xie, T., Wang, B., Wang, R., Cai, Y., Yuan, B., Gleber-Netto, F.O., Tian, X., Rodriguez-Rosario, A.E., Osman, A.A., et al. (2022). Mutant p53 drives an immune cold tumor immune microenvironment in oral squamous cell carcinoma. Commun. Biol. *5*, 757.
5. Bhatia, A., and Burtness, B. (2023). Treating Head and Neck Cancer in the Age of Immunotherapy: A 2023 Update. Drugs *83*, 217–248.
6. Ruffin, A.T., Li, H., Vujanovic, L., Zandberg, D.P., Ferris, R.L., and Bruno, T.C. (2023). Improving head and neck cancer therapies by immunomodulation of the tumour microenvironment. Nat. Rev. Cancer *23*, 173–188.
7. Wang, A., Dai, H., Gong, Y., Zhang, C., Shu, J., Luo, Y., Jiang, Y., Liu, W., and Bie, P. (2019). ANLN-induced EZH2 upregulation promotes pancreatic cancer progression by mediating miR-218-5p/LASP1 signaling axis. J. Exp. Clin. Cancer Res. *38*, 347.
8. Kucera, O., Siahaan, V., Janda, D., Dijkstra, S.H., Pilatova, E., Zatecka, E., Diez, S., Braun, M., and Lansky, Z. (2021). Anillin propels myosin-independent constriction of actin rings. Nat. Commun. *12*, 4595.
9. Sun, L., Guan, R., Lee, I.J., Liu, Y., Chen, M., Wang, J., Wu, J.Q., and Chen, Z. (2015). Mechanistic insights into the anchorage of the contractile ring by anillin and Mid1. Dev. Cell *33*, 413–426.
10. Naydenov, N.G., Koblinski, J.E., and Ivanov, A.I. (2021). Anillin is an emerging regulator of tumorigenesis, acting as a cortical cytoskeletal scaffold and a nuclear modulator of cancer cell differentiation. Cell. Mol. Life Sci. *78*, 621–633.
11. Morris, R.G., Husain, K.B., Budnar, S., and Yap, A.S. (2020). Anillin: The First Proofreading-like Scaffold? Bioessays *42*, e2000055.
12. Hohmann, T., and Dehghani, F. (2019). The Cytoskeleton-A Complex Interacting Meshwork. Cells *8*, 362.

Figure 7. ANLN promotes PD-L1 expression via the MAPK/ERK signaling pathway and enhances anti-PD-1 therapy efficacy

(A) Schematic diagram of the *in vivo* experimental design and treatment protocol. Subcutaneous head and neck tumor models were established using Anln-deficient and wild-type mEER cells, followed by treatment with anti-PD-1 monoclonal antibody or IgG2a isotype control.

(B–D) Tumor volume and weight measurements in tumor-bearing mice after treatment with anti-PD-1 monoclonal antibody or IgG2a control.

(E) Body weight assessment across different treatment groups.

(F) Multiplex immunofluorescence staining in mouse tumor samples.

(G–I) Flow cytometry analysis. *Statistical significance is denoted as $*p < 0.05$, $**p < 0.01$, $***p < 0.001$. Data are represented as mean with SD.

13. Lian, Y.F., Huang, Y.L., Wang, J.L., Deng, M.H., Xia, T.L., Zeng, M.S., Chen, M.S., Wang, H.B., and Huang, Y.H. (2018). Anillin is required for tumor growth and regulated by miR-15a/miR-16-1 in HBV-related hepatocellular carcinoma. Aging (Albany NY) *10*, 1884–1901.

14. Zeng, S., Yu, X., Ma, C., Song, R., Zhang, Z., Zi, X., Chen, X., Wang, Y., Yu, Y., Zhao, J., et al. (2017). Transcriptome sequencing identifies ANLN as a promising prognostic biomarker in bladder urothelial carcinoma. Sci. Rep. *7*, 3151.

15. Piekny, A.J., and Maddox, A.S. (2010). The myriad roles of Anillin during cytokinesis. Semin. Cell Dev. Biol. *21*, 881–891.

16. Lens, S.M.A., and Medema, R.H. (2019). Cytokinesis defects and cancer. Nat. Rev. Cancer *19*, 32–45.

17. Tuan, N.M., and Lee, C.H. (2020). Role of Anillin in Tumour: From a Prognostic Biomarker to a Novel Target. Cancers *12*, 1600.

18. Magnusson, K., Gremel, G., Rydén, L., Pontén, V., Uhlén, M., Dimberg, A., Jirström, K., and Pontén, F. (2016). ANLN is a prognostic biomarker independent of Ki-67 and essential for cell cycle progression in primary breast cancer. BMC Cancer *16*, 904.

19. Wang, D., Naydenov, N.G., Dozmorov, M.G., Koblinski, J.E., and Ivanov, A.I. (2020). Anillin regulates breast cancer cell migration, growth, and metastasis by non-canonical mechanisms involving control of cell stemness and differentiation. Breast Cancer Res. *22*, 3.

20. Suzuki, C., Daigo, Y., Ishikawa, N., Kato, T., Hayama, S., Ito, T., Tsuchiya, E., and Nakamura, Y. (2005). ANLN plays a critical role in human lung carcinogenesis through the activation of RHOA and by involvement in the phosphoinositide 3-kinase/AKT pathway. Cancer Res. *65*, 11314–11325.

21. Pandi, N.S., Manimuthu, M., Harunipriya, P., Murugesan, M., Asha, G.V., and Rajendran, S. (2014). In silico analysis of expression pattern of a Wnt/beta-catenin responsive gene ANLN in gastric cancer. Gene *545*, 23–29.

22. Wang, G., Shen, W., Cui, L., Chen, W., Hu, X., and Fu, J. (2016). Overexpression of Anillin (ANLN) is correlated with colorectal cancer progression and poor prognosis. Cancer Biomark. *16*, 459–465.

23. Zhang, S., Nguyen, L.H., Zhou, K., Tu, H.C., Sehgal, A., Nassour, I., Li, L., Gopal, P., Goodman, J., Singal, A.G., et al. (2018). Knockdown of Anillin Actin Binding Protein Blocks Cytokinesis in Hepatocytes and Reduces Liver Tumor Development in Mice Without Affecting Regeneration. Gastroenterology *154*, 1421–1434.

24. Guo, E., Mao, X., Wang, X., Guo, L., An, C., Zhang, C., Song, K., Wang, G., Duan, C., Zhang, X., et al. (2021). Alternatively spliced ANLN isoforms synergistically contribute to the progression of head and neck squamous cell carcinoma. Cell Death Dis. *12*, 764.

25. Horton, B.L., Morgan, D.M., Momin, N., Zagorulya, M., Torres-Mejia, E., Bhandarkar, V., Wittrup, K.D., Love, J.C., and Spranger, S. (2021). Lack of CD8(+) T cell effector differentiation during priming mediates checkpoint blockade resistance in non-small cell lung cancer. Sci. Immunol. *6*, eabi8800.

26. Long, J., Chen, P., Yang, X., Bian, J., Yang, X., Wang, A., Lin, Y., Wang, H., Sang, X., and Zhao, H. (2023). Co-expression of receptor tyrosine kinases and CD8 T-lymphocyte genes is associated with distinct prognoses, immune cell infiltration patterns and immunogenicity in cancers. Transl. Res. *256*, 14–29.

27. Choi, J.H., Lee, B.S., Jang, J.Y., Lee, Y.S., Kim, H.J., Roh, J., Shin, Y.S., Woo, H.G., and Kim, C.H. (2023). Single-cell transcriptome profiling of the stepwise progression of head and neck cancer. Nat. Commun. *14*, 1055.

28. Lambrechts, D., Wauters, E., Boeckx, B., Aibar, S., Nittner, D., Burton, O., Bassez, A., Decaluwé, H., Pircher, A., Van den Eynde, K., et al. (2018). Phenotype molding of stromal cells in the lung tumor microenvironment. Nat. Med. *24*, 1277–1289.

29. Dai, Y., Wang, Z., Xia, Y., Li, J., Wu, Y., Wang, Y., Jiang, H., and Cheng, J. (2023). Integrative Single-Cell and Bulk Transcriptomes Analyses Identify Intrinsic HNSCC Subtypes with Distinct Prognoses and Therapeutic Vulnerabilities. Clin. Cancer Res. *29*, 2845–2858.

30. Park, J.I. (2023). MAPK-ERK Pathway. Int. J. Mol. Sci. *24*, 9666.

31. Barbosa, R., Acevedo, L.A., and Marmorstein, R. (2021). The MEK/ERK Network as a Therapeutic Target in Human Cancer. Mol. Cancer Res. *19*, 361–374.

32. Gao, Z., Chen, J.F., Li, X.G., Shi, Y.H., Tang, Z., Liu, W.R., Zhang, X., Huang, A., Luo, X.M., Gao, Q., et al. (2022). KRAS acting through ERK signaling stabilizes PD-L1 via inhibiting autophagy pathway in intrahepatic cholangiocarcinoma. Cancer Cell Int. *22*, 128.

33. Liu, Z., Zhao, K., Wei, S., Liu, C., Zhou, J., Gou, Q., Wu, X., Yang, Z., Yang, Y., Peng, Y., et al. (2020). ROS1-fusion protein induces PD-L1 expression via MEK-ERK activation in non-small cell lung cancer. OncoImmunology *9*, 1758003.

STAR★METHODS

KEY RESOURCES TABLE

REAGENT or RESOURCE	SOURCE	IDENTIFIER
Antibodies		
Anti-Anillin antibody	Abcam	Cat#ab211872; RRID: AB_2756815
MEK1/2 antibody	Proteintech	Cat#11049-1-AP; RRID: AB_2140649
Phospho-MEK1 (Thr292) Antibody	Proteintech	Cat#28930-1-AP; RRID: AB_2918216
ERK1/2 antibody	Proteintech	Cat#11257-1-AP; RRID: AB_2139822
Phospho-ERK1/2 (Thr202/Tyr204) antibody	Proteintech	Cat#28733-1-AP; RRID: AB_2881202
GAPDH antibody	Proteintech	Cat#60004-1-Ig; RRID: AB_2107436
GZMB antibody	Proteintech	Cat#13588-1-AP; RRID: AB_2882205
CD8 antibody	Proteintech	Cat#66868-1-Ig; RRID: AB_2114429
PD-L1 (E1L3N) XP Rabbit Antibody	Cell Signaling Technology	Cat#13684; RRID: AB_2687655
Anti-rabbit IgG, HRP-linked Antibody	Cell Signaling Technology	Cat#7074S; RRID: AB_2099233
Anti-mouse IgG, HRP-linked Antibody	Cell Signaling Technology	Cat#7076S; RRID: AB_330924
Biological samples		
Mouse tumor tissue	This study	N/A
Human laryngeal carcinoma tissue	This study	N/A
Chemicals, peptides, and recombinant proteins		
RPMI 1640	Gibco	Cat# 12633020
IMDM	Gibco	Cat# 31980030
DMEM	Gibco	Cat# 11965092
DMEM/F12	Gibco	Cat# A4192001
Opti-MEM	Gibco	Cat# 31985070
Fetal Bovine Serum	Gibco	Cat# A5256701
Hydrocortisone	MedChemExpress	Cat# HY-N0583
Transferrin protein, mouse	MedChemExpress	Cat# HY-P73453
Insulin-1 protein	MedChemExpress	Cat# HY-P71805
Triiodothyronine	MedChemExpress	Cat# HY-A0070A
EGF protein, mouse	MedChemExpress	Cat# HY-P70590
Penicillin/Streptomycin	NCM Biotech	Cat# C100C5
Penicillin/Streptomycin	Biosharp	Cat# BL505A
TRIzol reagent	Invitrogen	Cat# 15596018
EDTA	Invitrogen	Cat# AM9260G
Anti–mouse PD-1	Bio X Cell	Cat# BE0146
Mouse IgG2a isotype control	Bio X Cell	Cat# BE0085
Deoxyribonuclease I	Sigma	Cat# DN25-1G
Opal 7-Color Automation IHC Kit	Akoya Biosciences	Cat # NEL821001KT
DNase/RNase-Free Water	Solarbio	Cat# R1600
Phosphate Buffered Saline	Solarbio	Cat# P1020
Lipofectamine™ 3000 Transfection Reagent	Thermo Fisher	Cat# L3000015
Trypsin	Thermo Fisher	Cat# 25200056
First Strand cDNA Synthesis Kit	TOYOBO	Cat# FSK-101
SYBR Green Real-time PCR Master Mix-Plus-	TOYOBO	Cat# QPK-212

(*Continued on next page*)

Continued

REAGENT or RESOURCE	SOURCE	IDENTIFIER
Deposited data		
Raw and analyzed data, see Table S2	This paper	N/A
Experimental models: Cell lines		
AMC-HN-8	ATCC	RRID: CVCL_5966
FaDu	ATCC	RRID: CVCL_1218
NOK-SI	ATCC	RRID: CVCL_BW57
SCC-4	ATCC	RRID: CVCL_1684
mEER	ATCC	RRID: CVCL_B6J2
Tu212	ATCC	RRID: CVCL_4915
DOK	ATCC	RRID: CVCL_1180
Experimental models: Organisms/strains		
C57BL/6 mice	Vital River Laboratory Animal Technology (Beijing, China)	N/A
Oligonucleotides		
Primers for quantitative PCR, see Table S3	This paper	N/A
siRNA/shRNA targeting sequence, see Table S4	This paper	N/A
Software and algorithms		
ImageJ software	National Institutes of Health	N/A
FlowJo v10.8.1 software	FlowJo LLC	N/A
GraphPad Prism 7.0	GraphPad Software	N/A
SPSS version 25	SPSS Software	N/A
R 4.2.0	R software	N/A

EXPERIMENTAL MODEL AND STUDY PARTICIPANT DETAILS

Ethics approval and consent to participate

The study was approved by the Institutional of Research Board of [Harbin Medical University], with the approval number [HMUIRB2022020]. All participants provided written informed consent prior to their inclusion in the study, in accordance with the Declaration of Helsinki.

Cell culturing

DOK cells were grown in 1640 medium. Tu212 cells were cultured in IMDM medium, and mEER cells were cultured in a mixed medium composed of DMEM, F12, Fetal Bovine Serum, and additional supplements including hydrocortisone, transferrin, insulin, triiodothyronine, and mouse EGF. The NOK, FaDu, AMC-HN-8, and SCC-4 cell lines were cultured in DMEM medium. All media were supplemented with 10% fetal bovine serum and 1% Penicillin/Streptomycin. The mouse HNSCC cell line mEER was generously provided by Dr. Xueying Wang (Department of Otolaryngology-Head and Neck Surgery, Xiangya Hospital, Central South University, China). All cell lines were maintained at 37°C in a 5% CO_2 atmosphere and were routinely tested for mycoplasma contamination, confirming negative results. All experiments were performed with mycoplasma-free cells.

Mouse tumor model and treatment

The animal study protocol was approved by the Ethics Committee of Harbin Medical University Cancer Hospital. C57BL/6 mice, aged 4–6 weeks, were sourced from Vital River Laboratory Animal Technology (Beijing, China), and maintained under standard laboratory conditions with proper food and water. For tumor model development, ANLN knockdown or control mEER cells (1×10^{-6}) were subcutaneously injected into the dorsal flank of each mouse. After a period of three weeks, the mice were euthanized, and the tumors were harvested for weighing. In the combination treatment evaluation group, seven days post-inoculation, mice received 100μg of anti–mouse PD-1 or a mouse IgG2a isotype control via intraperitoneal injection (100 mg/injection every 3 days). Tumor volume was assessed employing the formula: the product of length and the square of width divided by two, with length denoting the utmost diameter of the tumor and width indicating the minimal diameter.

METHOD DETAILS

Quantitative Real-Time PCR (qRT-PCR)

Total RNA was extracted using TRIzol reagent following the manufacturer's instructions, and cDNA synthesis was performed using the First Strand cDNA Synthesis Kit. qRT-PCR was conducted using SYBR Green Real-time PCR Master Mix-Plus-on a CFX96 Real-Time PCR Detection System (Bio-Rad, USA).

Opal multiplex immunohistochemistry

Formalin-fixed, paraffin-embedded sections were deparaffinized, rehydrated, and treated with 3% hydrogen peroxide for 30 min. Heat-induced epitope retrieval was performed using citrate buffer (pH 6.0) at 95°C for 5 min. Imaging was done using the Vectra Polaris Automated Quantitative Pathology Imaging System and analyzed with inForm Tissue Finder and phenoptr software.

Immunohistochemistry

Formalin-fixed, paraffin-embedded HNSCC tissue samples (n = 110) from the Cancer Hospital of Harbin Medical University were stained for ANLN and CD8 expression. Tissue sections were incubated with primary antibodies overnight at 4°C, followed by HRP-conjugated goat anti-rabbit secondary antibody incubation for 30 min at room temperature. Staining was developed with DAB and counterstained with hematoxylin. Staining intensity and percentage of positive tumor cells were scored by two pathologists independently, with a Histo score ranging from 0 to 300%.

Western blotting

Protein extraction was followed by SDS-PAGE and transfer onto PVDF membranes. Membranes were blocked with 5% skim milk in PBST for 1 h at room temperature. After blocking, membranes were incubated with primary antibodies overnight at 4°C, followed by HRP-conjugated secondary antibodies for 45 min at room temperature. Bands were visualized using ECL.

Migration assay

Cells (3 × 10^4/well) were seeded in serum-free DMEM in the upper chamber of Transwell inserts (8 μm pore size). The lower chamber contained DMEM with 10% FBS as a chemoattractant. After 48 h at 37°C in a 5% CO_2 incubator, migrated cells on the lower side of the insert were fixed with 4% paraformaldehyde, stained with 0.1% crystal violet, and imaged under a microscope.

Wound healing assay

AMC-HN-8 and SCC-4 cells were cultured in 6-well plates until 95% confluent. A scratch was made across the monolayer with a pipette tip. Cells were washed with PBS and cultured in serum-free DMEM. Images were captured at 0 and 24 h to measure wound closure.

Survival analysis

The Kaplan-Meier method was used to assess the relationship between the target gene expression and patient survival. Patients were divided into high-expression and low-expression groups based on gene expression levels, and the log rank test was used to evaluate the differences in survival curves between the two groups. We also conducted univariate and multivariate Cox proportional hazards regression analyses to control for potential confounding variables (such as age, gender, and clinical stage) and calculated the hazard ratios (HR) with their 95% confidence intervals.

Single-cell analysis

Single-cell transcriptome analysis was conducted on 20 tissue samples from primary tumors (CA, n = 20). Single-cell RNA sequencing data were obtained from the GSE181919 dataset and processed using the Seurat package. The single-cell data were initially filtered, normalized, and corrected for batch effects. Subsequently, dimensionality reduction was conducted using Principal Component Analysis (PCA), followed by UMAP visualization. Cell subclusters were identified using the FindClusters function, with annotations assigned to different cell subpopulations. Finally, the expression levels of the target gene were analyzed across various cell subpopulations.

ESTIMATE score calculation and comparison

The ESTIMATE algorithm was applied to evaluate the immune infiltration and stromal content in tumor samples. This algorithm computes three scores for each sample: the Immune Score, Stromal Score, and ESTIMATE Score (a combination of immune and stromal scores), which reflect the levels of immune and stromal components within the tumor microenvironment. The ESTIMATE scores were calculated using the ''estimate'' package in R (version 4.2.0).

QUANTIFICATION AND STATISTICAL ANALYSIS

Statistical analysis was conducted using SPSS version 25 (SPSS, Inc., Chicago, IL, USA). The experimental results obtained in both *in vitro* and *in vivo* settings were expressed as the mean ± standard deviation (SD). To assess differences between two groups, the Student's t-test was employed. When comparing multiple groups, either one-way or two-way analysis of variance (ANOVA) was performed, followed by post hoc Student-Neuman-Keuls (SNK) tests to establish means separation. Differential gene expression analysis of cancerous and paracancerous tissues was performed using the wilcox test. Statistical significance was considered achieved at a significance level of $p < 0.05$. Bioinformatic analysis was carried out using R software (version 4.1.0; https://www.r-project.org/). P-value <0.05 were considered statistically significant. The symbol * indicates $p < 0.05$, the symbol ** represents $p < 0.01$, and the symbol *** represents $p < 0.001$.